Abstract

In this paper, the heat transfer from a single heat fin to the air flow in the wake of a piezoelectric fan (piezofan) is optimised. Both the heat fin and the piezofan are positioned in a channel, which has a significant influence on the flow field. The design variable is the frequency of the voltage applied to the piezofan. The heat transfer for different excitation frequencies is calculated using unsteady fluid-structure interaction simulations. To obtain a modular simulation environment, the flow equations and the structural equations are solved separately. However, the equilibrium on the fluid-structure interface is not satisfied automatically in this partitioned approach. Therefore, the interface quasi-Newton technique with an approximation for the inverse of the Jacobian from a least-squares model (IQN-ILS) is used to perform coupling iterations between the flow solver and the structural solver in each time step. With the unsteady fluid-structure interaction model, a surrogate model is constructed. The optimization of the surrogate model yields a frequency close to the first eigenfrequency of the structure.

Keywords: piezofan, fluid-structure interaction, partitioned solution, IQN-ILS, optimization, heat fins.

1 Introduction

In the last decade, the simulation of fluid-structure interaction has gained interest. With the currently available simulation techniques, also a piezoelectric fan (or piezofan) can be simulated. Figure 1 depicts a bimorph piezofan [1]. Such a piezofan consists of a thin, passive plate which is clamped at one end. The top and bottom of this plate are partially covered by a thin patch of piezoelectric material. By applying alternating voltages with a phase shift of 180 degrees to the patches, one of the

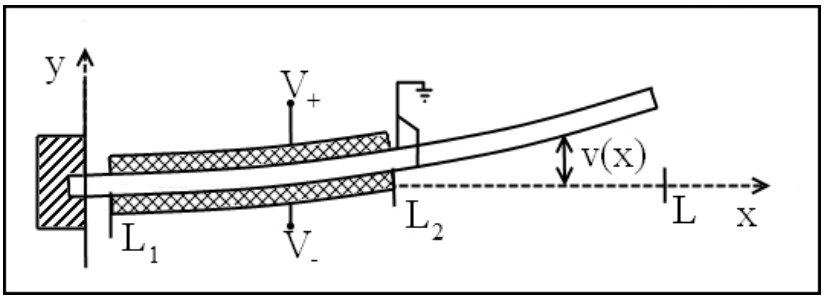

Figure 1: A sketch of a bimorph piezofan with the definition of the parameters L_1, L_2 and L. The passive plate is white, the piezoelectric patches are cross-hatched and the clamping is hatched.

patches expands in the direction parallel to the plate while the other one contracts in that same direction. Due to these small but opposite deformations of the patches on its top and bottom, the elastic plate bends, resulting in a significant motion of the free end in the y-direction. If the excitation frequency is close to the resonance frequency of the plate, the oscillation amplitude is relatively large. The interaction between the piezofan and the surrounding air induces an air flow from the clamped end towards the free end. Consequently, piezofans can be used to cool electronic components. Piezofans are an alternative to conventional rotating fans as their power consumption is an order of magnitude smaller [2]. Moreover, they produce less noise, given that the eigenfrequencies lie well outside of the hearing range [3].

In this paper, a fluid-structure interaction model for a piezofan with a single heat fin in its wake is used in an optimization study. The fluid-structure interaction is calculated in a partitioned way, which means that the flow equations and the structural equations are solved separately. Nevertheless, the equilibrium of the velocity and stress on the fluid-structure interface is enforced in each time step of the unsteady simulations by performing coupling iterations between the flow solver and the structural solver. For the coupling iterations, the interface quasi-Newton technique with an approximation for the inverse of the Jacobian from a least-squares model (IQN-ILS) is used [4].

Although piezofans have been optimised before without any confinement [5] or enclosed in a box [3], a piezofan has never been optimised in a channel as presented in this paper. The model with a piezofan and a heat fin in a channel is a simplification of a piezofan embedded in a device that contains electronic components. Moreover, the complete fluid-structure interaction is taken into account in the unsteady simulations for the optimization, so without neglecting the influence of the fluid on the structure. In the optimization, the design variable is the frequency of the alternating voltage that is applied to the patches of the piezofan and the objective is the time-averaged heat transfer from the left-hand side of the fin towards the surrounding air.

The remainder of this paper is organised as follows. In Section 2, the model for the structural deformation and for the flow field are described and validated, followed by

a summary of the coupling technique in Section 3. The optimization and its results are given in Section 4.

2 Description and validation of the models

2.1 Structural model

The linear constitutive equations between the strain S, the stress T, the electric field E and the electric charge density displacement D in a piezoelectric material are given by

$$S = s^E \cdot T + d^t \cdot E \tag{1a}$$
$$D = d \cdot T + \epsilon^T \cdot E \tag{1b}$$

with t denoting a transpose. s^E is the short-circuited (i.e. $E = 0$) elastic compliance and ϵ^T is the free (i.e. $T = 0$) dielectric permittivity. The mechanic and electric variables are coupled by the electro-mechanical coupling d. In matrix-vector notation, Equations (1) are given by

$$\begin{bmatrix} S_{11} \\ S_{22} \\ S_{33} \\ S_{23} \\ S_{13} \\ S_{12} \end{bmatrix} = \begin{bmatrix} s^E_{11} & s^E_{12} & s^E_{13} & 0 & 0 & 0 \\ s^E_{21} & s^E_{22} & s^E_{23} & 0 & 0 & 0 \\ s^E_{31} & s^E_{32} & s^E_{33} & 0 & 0 & 0 \\ 0 & 0 & 0 & s^E_{44} & 0 & 0 \\ 0 & 0 & 0 & 0 & s^E_{55} & 0 \\ 0 & 0 & 0 & 0 & 0 & s^E_{66} \end{bmatrix} \cdot \begin{bmatrix} T_{11} \\ T_{22} \\ T_{33} \\ T_{23} \\ T_{13} \\ T_{12} \end{bmatrix} + \begin{bmatrix} 0 & 0 & d_{31} \\ 0 & 0 & d_{32} \\ 0 & 0 & d_{33} \\ 0 & d_{24} & 0 \\ d_{15} & 0 & 0 \\ 0 & 0 & 0 \end{bmatrix} \cdot \begin{bmatrix} E_1 \\ E_2 \\ E_3 \end{bmatrix} \tag{2a}$$

$$\begin{bmatrix} D_1 \\ D_2 \\ D_3 \end{bmatrix} = \begin{bmatrix} 0 & 0 & 0 & 0 & d_{15} & 0 \\ 0 & 0 & 0 & d_{24} & 0 & 0 \\ d_{31} & d_{32} & d_{33} & 0 & 0 & 0 \end{bmatrix} \cdot \begin{bmatrix} T_{11} \\ T_{22} \\ T_{33} \\ T_{23} \\ T_{13} \\ T_{12} \end{bmatrix} + \begin{bmatrix} \epsilon^T_{11} & 0 & 0 \\ 0 & \epsilon^T_{22} & 0 \\ 0 & 0 & \epsilon^T_{33} \end{bmatrix} \cdot \begin{bmatrix} E_1 \\ E_2 \\ E_3 \end{bmatrix} \tag{2b}$$

The structure is discretised using the finite element method (FEM). The structure is meshed using 114 quadratic 8-node plane stress continuum elements with reduced integration. The mesh nearby the clamped end of the piezofan is shown in Figure 2. The dimensions and material properties are listed in Table 1.

Geometric nonlinearity is taken into account during the solution process and the stress on the fluid-structure interface follows the rotation of the structure during the time step. Unconditionally stable implicit Hilber-Hughes-Taylor time integration [6] is used with a small numerical damping parameter $\alpha_s = -0.05$. If $L_2 = 22$mm, the first eigenfrequency is 138Hz which corresponds with a period of 7.2ms. As the excitation frequency will be close to the first eigenfrequency, the time step is set to 72μs, which is divided into increments of 1μs.

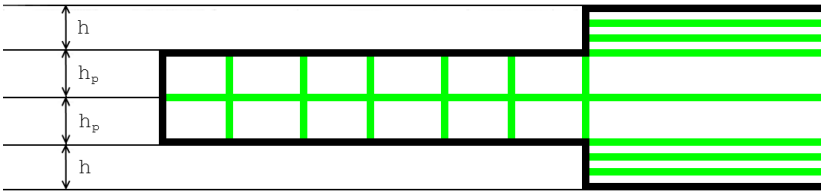

Figure 2: A detail of the structural mesh with the definition of the parameters h and h_p. The leftmost edge is clamped.

Symbol	Value
h	0.178mm
h_p	0.0508mm
$\rho_{passive}$	8400kg/m^3
$E_{passive}$	100GPa
L_1	0.5mm
L	27.424mm
ρ_{piezo}	7800kg/m^3
ϵ_{piezo}	3800C/Vm
E_{piezo1}	62GPa
E_{piezo2}	62GPa
E_{piezo3}	62GPa

Symbol	Value
$\nu_{piezo12}$	-0.372
$\nu_{piezo13}$	0.372
$\nu_{piezo23}$	-0.3
$G_{piezo12}$	20GPa
$G_{piezo13}$	23.646GPa
$G_{piezo23}$	20GPa
d_{31}	-0.19nC/N
d_{32}	0.32nC/N
d_{33}	0.19nC/N
d_{24}	0.58nC/N
d_{15}	0.58nC/N

Table 1: The dimensions and properties of the passive and piezoelectric material in the structural model [5].

L_2		7mm	14mm	21mm
First	Analytical	122Hz	191Hz	164Hz
	Numerical	121Hz	187Hz	161Hz
	Error	0.8%	2.1%	1.9%
Second	Analytical	600Hz	494Hz	1269Hz
	Numerical	593Hz	490Hz	1245Hz
	Error	1.2%	0.8%	1.9%

Table 2: The open-circuited first and second eigenfrequency for different values of L_2. The error is the relative difference compared to the analytical results from Bürmann et al. [5].

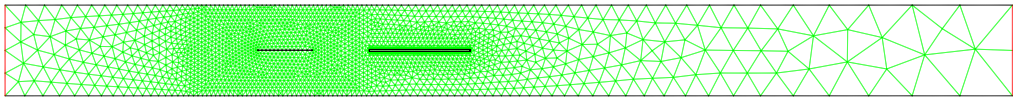

Figure 3: The fluid mesh of the channel with the piezofan (left) and a heat fin (right).

To validate the structural model, the first and second eigenfrequency for different values of L_2 are calculated and compared with analytical results from Bürmann et al. [5]. In these calculations, the voltage on the piezoelectric patches is generated naturally by the bending (open-circuited or OC). The result of this comparison can be found in Table 2. The maximal difference between the numerical results and the analytical results is 1.9%.

2.2 Fluid model

The piezofan and the heat fin in its wake are located in a channel of 500mm long and 45mm high. The heat fin of 50mm long and 1mm thick [7] is positioned 30mm behind the piezofan. The air is considered as an incompressible fluid. For the turbulence, the one-equation vorticity based Spalart-Allmaras model [8] is used. The mesh initially contains 9090 triangular cells (see Figure 3). The cell size is small in the neighbourhood of the piezofan and the heat fin and it increases towards the inlet and outlet of the channel. The top and bottom of the channel are no-slip walls. Zero pressure, a temperature of 300K and a modified turbulent viscosity of $0.001\text{m}^2/\text{s}$ are imposed at the left and right end of the channel.

The boundary of the heat fin is a no-slip wall at 333K. The temperature of the fin is imposed instead of the heat flux as a constant heat flux over the fin is unphysical. The mean temperature of the thermal boundary layer will increase in the direction of the flow, so that the heat flux to the flow decreases. By contrast, a constant temperature of the fin is possible, if the material of the heat fin is assumed to be ideal in terms of heat

conductivity.

The equations for the conservation of mass, momentum and energy together with the equation for kinematic turbulent viscosity are discretised in arbitrary Lagrangian-Eulerian (ALE) formulation using the finite volume method (FVM). Scalars are stored in the cell centres and a power law is used to obtain momentum variables at the faces. Gradients at the cell centres are calculated from the face values using the Green-Gauss theorem. The face values for the gradient calculations are the arithmetic average of the node values, which are in turn the weighted average of the values in the cells around the node. The pressure interpolation at the faces is performed with a staggered approach. The flow equations are solved using the pressure-implicit with splitting of operators (PISO) scheme with skewness and neighbour correction. Algebraic multi-grid (AMG) is employed to accelerate the convergence.

The mesh of the fluid domain in a box around the piezofan is deforming, driven by the deformation of the fluid-structure interface. The displacement u of the fluid mesh in the x- and y-direction is determined by solving Laplace equations

$$\Delta u_x = 0 \tag{3a}$$

$$\Delta u_y = 0. \tag{3b}$$

On the outer boundaries of the box around the piezofan, the boundary condition $u_{x,y} = 0$ is applied while $u_{x,y}$ is prescribed by the coupling algorithm on the boundaries of the piezofan. After this displacement of the mesh, smoothing with fictitious springs between the mesh nodes is performed. Cells which have either become too skewed or which fall outside the range of desired cell sizes are eliminated once in each time step. As a result, the number of cells varies slightly during the simulation. The implicit finite difference time discretisation is first-order accurate on the moving mesh. The flow field is initially at rest and at a temperature of 300K. The same time step as for the structure is used, namely 72μs.

3 Fluid-structure interaction

In this section, the structural model and the flow model are coupled using the IQN-ILS algorithm [4]. The coupling technique is called IQN-ILS because it calculates the **i**nterface position using **q**uasi-**N**ewton iterations with an approximation for the **i**nverse of the Jacobian from a **l**east-**s**quares model. The coupling technique will be described below, after some definitions.

3.1 Definitions

The function

$$\boldsymbol{y} = \mathcal{F}(\boldsymbol{x}) \tag{4}$$

is referred to as the flow solver. The vector $\boldsymbol{x}$ is the displacement of the fluid-structure interface and the vector $\boldsymbol{y}$ is the stress distribution on the interface. The structural

solver is represented as

$$\boldsymbol{x} = \mathcal{S}(\boldsymbol{y}). \tag{5}$$

These abstract definitions of the flow solver and structural solver emphasize that they are treated as black boxes. The solvers calculate the solution of the flow equations and the structural equations in the entire fluid and structural domain. However, the input and output of the solver is limited to the fluid-structure interface. The dependence on information from previous time steps is omitted. The FSI problem is reformulated as

$$\boldsymbol{x} = \mathcal{S} \circ \mathcal{F}(\boldsymbol{x}) \tag{6}$$

or equivalently

$$\mathcal{R}(\boldsymbol{x}) = \mathcal{S} \circ \mathcal{F}(\boldsymbol{x}) - \boldsymbol{x} = \boldsymbol{0} \tag{7}$$

with $\mathcal{R}$ the residual operator.

In the remainder of this section, all values and functions are at the new time level $n+1$, unless indicated otherwise with a left superscript. A right superscript indicates the coupling iteration in the time step. Capital letters are matrices and bold lower case letters are vectors. Approximations are indicated with a hat. The output of the solvers $\mathcal{F}$ and $\mathcal{S}$ is indicated with a tilde because this is only an intermediate value that is not passed on to the next coupling iteration. This tilde is dropped once the final value that will be used in the next iteration has been calculated. The equality sign can be both an assignment or an equality. The coupling iterations begin from an extrapolation

$$\boldsymbol{x}^{n+1} = \frac{5}{2}\boldsymbol{x}^{n} - 2\boldsymbol{x}^{n-1} + \frac{1}{2}\boldsymbol{x}^{n-2} \tag{8}$$

of the interface's displacement.

3.2 Coupling technique

Equation (7) is a set of nonlinear equations in the interface displacement, which can be solved by means of Newton-Raphson iterations

$$\text{solve } \mathcal{R}'^{k} \Delta \boldsymbol{x}^{k} = -\boldsymbol{r}^{k} \tag{9a}$$

$$\boldsymbol{x}^{k+1} = \boldsymbol{x}^{k} + \Delta \boldsymbol{x}^{k} \tag{9b}$$

with $\mathcal{R}'^{k}$ the Jacobian of $\mathcal{R}$ at$\boldsymbol{x}^{k}$. The residual is calculated as

$$\boldsymbol{r}^{k} = \mathcal{R}(\boldsymbol{x}^{k}) = \mathcal{S} \circ \mathcal{F}(\boldsymbol{x}^{k}) - \boldsymbol{x}^{k} = \tilde{\boldsymbol{x}}^{k} - \boldsymbol{x}^{k}. \tag{10}$$

The convergence criterion for the Newton-Raphson iterations is $||\boldsymbol{r}^{k}||_2 \leq \epsilon_o$ with ϵ_o the convergence tolerance. However, the exact Jacobian of $\mathcal{R}$ is unknown because the Jacobians of $\mathcal{F}$ and $\mathcal{S}$ are unavailable. Moreover, the linear system in Equation (9a) with as dimension the number of degrees of freedom in the displacement of the fluid-structure interface has to be solved in every Newton-Raphson iteration.

Degroote et al. [4] developed an approximation for the product of the inverse of the Jacobian with a vector, based on the least-squares technique of Vierendeels et al. [9]. With this approximation, Equation (9a) becomes

$$\boldsymbol{x}^{k+1} = \boldsymbol{x}^k + \widehat{\left(\mathcal{R}'^k\right)}^{-1} \left(-\boldsymbol{r}^k\right). \tag{11}$$

The matrix-vector product is calculated from data obtained during the previous quasi-Newton iterations. At the end of coupling iteration k, the vectors $\boldsymbol{r}^i$ and the corresponding vectors $\tilde{\boldsymbol{x}}^i$ ($i = 0, \ldots, k$) are known. The IQN-ILS-algorithm calculates the differences between vectors from consecutive coupling iteration

$$\Delta\boldsymbol{r}^{i-1} = \boldsymbol{r}^i - \boldsymbol{r}^{i-1} \tag{12a}$$

$$\Delta\tilde{\boldsymbol{x}}^{i-1} = \tilde{\boldsymbol{x}}^i - \tilde{\boldsymbol{x}}^{i-1} \tag{12b}$$

This results in a set of differences $\Delta\boldsymbol{r}^i$ and a corresponding set of differences $\Delta\tilde{\boldsymbol{x}}^i$ ($i = 0, \ldots, k-1$), which grow in each coupling iteration. These vectors can be stored as the columns of the matrices

$$\boldsymbol{V}^k = \begin{bmatrix} \Delta\boldsymbol{r}^{k-1} & \Delta\boldsymbol{r}^{k-2} & \ldots & \Delta\boldsymbol{r}^1 & \Delta\boldsymbol{r}^0 \end{bmatrix} \tag{13a}$$

$$\boldsymbol{W}^k = \begin{bmatrix} \Delta\tilde{\boldsymbol{x}}^{k-1} & \Delta\tilde{\boldsymbol{x}}^{k-2} & \ldots & \Delta\tilde{\boldsymbol{x}}^1 & \Delta\tilde{\boldsymbol{x}}^0 \end{bmatrix}. \tag{13b}$$

The vector $\Delta\boldsymbol{r} = 0 - \boldsymbol{r}^k$ is approximated as a linear combination of the known $\Delta\boldsymbol{r}^i$ in $\boldsymbol{V}^k$

$$\Delta\boldsymbol{r} \approx \boldsymbol{V}^k \boldsymbol{c}^k \tag{14}$$

with $\boldsymbol{c}^k$ the decomposition coefficients. Equation (14) is an overdetermined set of equations because the number of rows of $\boldsymbol{V}^k$ is typically larger than the number of columns (if this is not the case, the rightmost columns $\boldsymbol{V}^k$ and $\boldsymbol{W}^k$ are discarded). Therefore, the least-squares solution to Equation (14) is calculated using the QR-decomposition of $\boldsymbol{V}^k$

$$\boldsymbol{V}^k = \boldsymbol{Q}^k \boldsymbol{R}^k, \tag{15}$$

which is calculated using Householder transformations [10]. The time required for this calculation is small in comparison to the time required for $\mathcal{S}$ and $\mathcal{F}$. Subsequently, the vector $\boldsymbol{c}^k$ is obtained by solving the system

$$\boldsymbol{R}^k \boldsymbol{c}^k = \left(\boldsymbol{Q}^k\right)^t \Delta\boldsymbol{r}. \tag{16}$$

The $\Delta\tilde{\boldsymbol{x}}$ corresponding to $\Delta\boldsymbol{r}$ is now calculated by making a linear combination of the known $\Delta\tilde{\boldsymbol{x}}^i$ in $\boldsymbol{W}^k$, analogous to Equation (14).

$$\Delta\tilde{\boldsymbol{x}} = \boldsymbol{W}^k \boldsymbol{c}^k \tag{17}$$

From Equation (10), it follows that

$$\Delta\boldsymbol{r} = \Delta\tilde{\boldsymbol{x}} - \Delta\boldsymbol{x}. \tag{18}$$

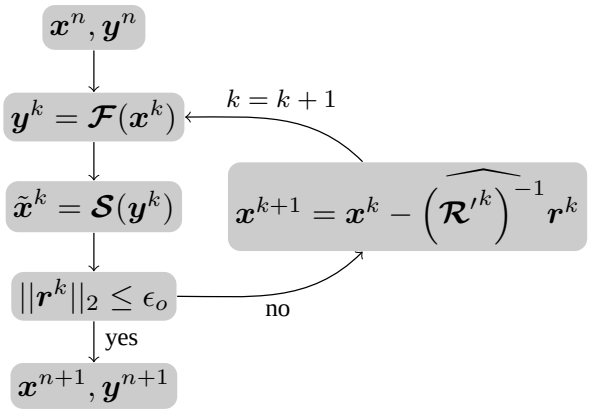

Figure 4: A scheme of the IQN-ILS coupling iterations within one time step.

Together, Equations (17) and (18) yield

$$\Delta \boldsymbol{x} = \boldsymbol{W}^k \boldsymbol{c}^k - \Delta \boldsymbol{r}, \tag{19}$$

the approximation for $\Delta \boldsymbol{x}$. As $\boldsymbol{c}^k$ is a function of $\boldsymbol{r}$, this is an approximation for the product of the inverse of the Jacobian with the vector $\Delta \boldsymbol{r} = -\boldsymbol{r}^k$. This procedure requires less memory and is faster than the explicit construction of the inverse of the Jacobian. The complete coupling scheme is shown in Figure 4. In this work, the convergence tolerance for the coupling iterations is defined as a fraction of the initial residual, namely $\epsilon_o = 10^{-3}||\boldsymbol{r}^0||_2$.

4 Optimization

The design variable in the optimization is the frequency f of the alternating voltage that is applied to the patches of the piezofan. The objective function that needs to be maximised is the time-averaged heat transfer h from the left-hand side of the fin towards the surrounding air. As the evaluation of the heat transfer for a given frequency requires a time-consuming unsteady FSI simulation, a surrogate model $\hat{h}(f)$ is first constructed, as will be explained below. This surrogate model is subsequently used for the actual optimization (see Figure 5).

The data set for the surrogate model is created by performing a simulation for $f = 75, 100, 150, 175$Hz. As these simulations are independent, they are run simultaneously, each on a different cluster node. In each of these simulations, the flow solver performs its calculation on 4 cores. The mesh of the structure proved to be too small to benefit from a parallel simulation. Figure 6 depicts the evolution of the heat transfer as a function of time, for the different excitation frequencies.

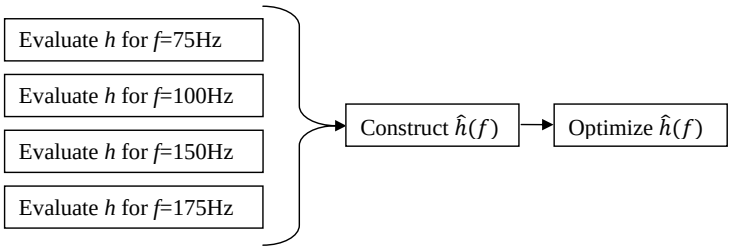

Figure 5: A scheme of the optimization process. First, a data set is constructed. Secondly, a surrogate model $\hat{h}(f)$ is constructed and, finally, this surrogate model is optimised.

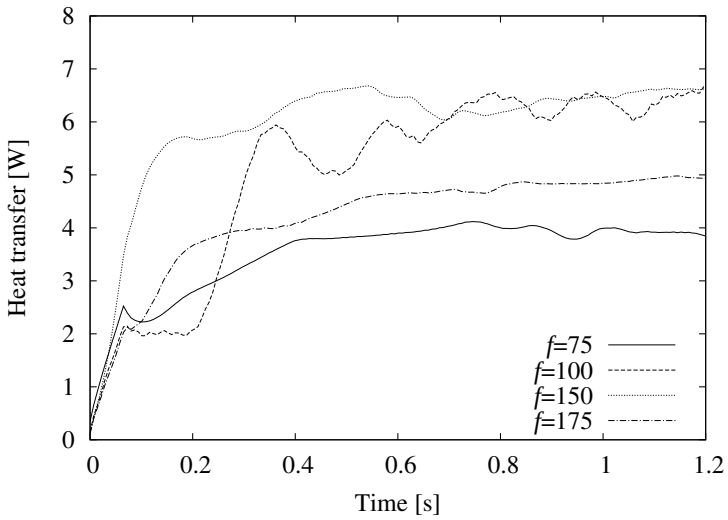

Figure 6: The heat transfer from the left-hand side of the fin towards the surrounding air as a function of time, for different excitation frequencies.

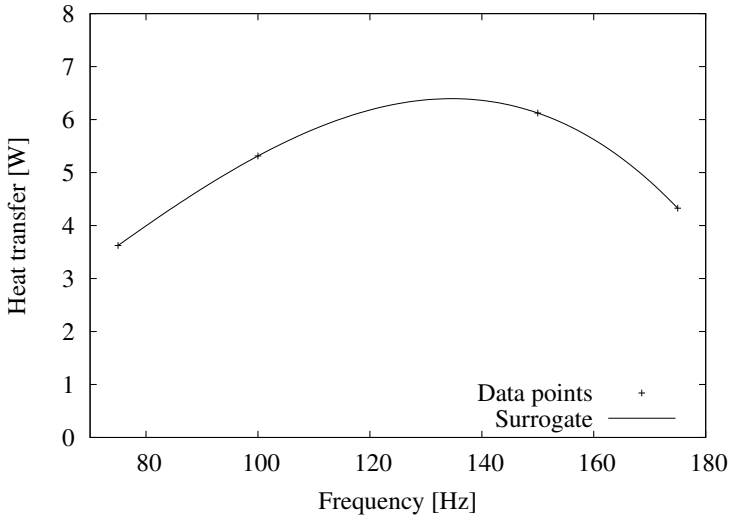

Figure 7: The data points and the surrogate model for the time-averaged heat transfer from the left-hand side of the fin towards the surrounding air as a function of the excitation frequency.

The time-averaged heat transfer h during the last 0.8s is calculated for each excitation frequency f, resulting in $N + 1 = 4$ data points (f_i, h_i). Then, a surrogate model $\hat{h}(f)$ is constructed using a cubic spline curve through these data points. The cubic spline interpolation consists of N cubic polynomials $\hat{h}_i(f)$ with coefficients $\hat{h}_{i,j}$ $(0 \leq j \leq 3)$.

$$\hat{h}(f) = \hat{h}_i(f) = \sum_{j=0}^{3} \hat{h}_{i,j}(f - f_i)^j \quad \forall f \in [f_i, f_{i+1}], 0 \leq i \leq N-1 \tag{20}$$

The coefficients are determined by the interpolation conditions, continuity conditions and continuity of the first and second derivative at the data points.

$$\hat{h}(f_i) = h_i \quad 0 \leq i \leq N \tag{21a}$$
$$\hat{h}_i(f_{i+1}) = \hat{h}_{i+1}(f_{i+1}) \quad 0 \leq i \leq N-2 \tag{21b}$$
$$\hat{h}'_i(f_{i+1}) = \hat{h}'_{i+1}(f_{i+1}) \quad 0 \leq i \leq N-2 \tag{21c}$$
$$\hat{h}''_i(f_{i+1}) = \hat{h}''_{i+1}(f_{i+1}) \quad 0 \leq i \leq N-2 \tag{21d}$$

Both the data points and the surrogate model are depicted in Figure 7.

The maximum of the surrogate model is calculated by searching the frequency for which its gradient equals zero.

$$\hat{h}'(f) = 0 \tag{22}$$

This equation is solved by performing Newton steps, using a central difference approximation to the gradient and Broyden-Fletcher-Goldfarb-Shanno (BFGS) updating

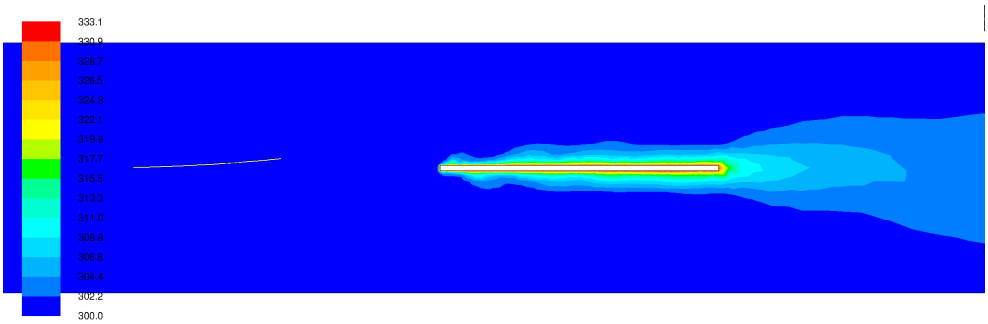

Figure 8: The temperature contours after 1.2s for $f = 138$Hz.

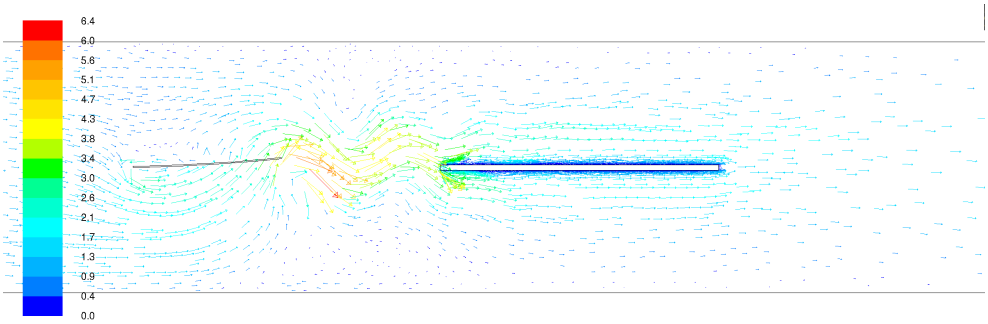

Figure 9: The velocity vectors after 1.2s for $f = 138$Hz.

of the hessian. The convergence of the optimization is determined by the criteria

$$\frac{|\Delta h|}{\max(1, |h|)} < 10^{-4} \tag{23a}$$

$$\frac{|\Delta f|}{\max(1, |f|)} < 10^{-4} \tag{23b}$$

$$|h'| < 10^{-3} \tag{23c}$$

which are all satisfied after 5 iterations, yielding $f = 134.62$Hz and $h = 6.39$W. However, in an additional FSI simulation with the excitation frequency equal to the first eigenfrequency of the piezofan, i.e. $f = 138$Hz, the time-averaged heat transfer was $h = 7.57$W. Hence, the frequency resulting from the optimization is close to the first eigenfrequency, but the resolution of the surrogate model should be refined to obtain a frequency closer to the first eigenfrequency.

Figures 8 and 9 depict temperature contours and velocity vectors, respectively, after 1.2s in the simulation with $f = 138$Hz. From these figures, it can be seen that the top and bottom wall of the channel constrain the vortices shed of by the piezofan. The flow over the heat fin is relatively uniform.

5 Conclusions

Unsteady fluid-structure interaction simulations of a piezofan with a heat fin in its wake have been performed. The time-averaged heat transfer has been optimised as a function of the excitation frequency. The optimization is performed on a surrogate model of the actual simulation, using a number of precomputed data points.

References

[1] M. Toda, "Theory of air flow generation by a resonant type PVF2 bimorph cantilever vibrator", *Ferroelect*, 22(3–4): 911–918, 1979.

[2] I. Sauciuc, "Piezo Actuators for Electronics Cooling", *Electronics Cooling*, 13 (1): 12–17, 2007.

[3] T. Açikalin, S. Garimella, A. Raman, J. Petroski, "Characterization and optimization of the thermal performance of miniature piezoelectric fans", *International Journal of Heat and Fluid Flow*, 28: 806–820, 2007.

[4] J. Degroote, K.J. Bathe, J. Vierendeels, "Performance of a new partitioned procedure versus a monolithic procedure in fluid-structure interaction", *Computers and Structures*, 87(11–12): 793–801, 2009.

[5] P. Bürmann, A. Raman, S. Garimella, "Dynamics and Topology Optimization of Piezoelectric Fans", *IEEE Transactions on Components and Packaging Technologies*, 25(4): 592–600, December 2003.

[6] H. Hilber, T. Hughes, R. Taylor, "Improved numerical dissipation for time integration algorithms in structural dynamics", *Earthquake Engineering & Structural Dynamics*, 5(3): 283–292, 1977.

[7] C.T. Chen, C.K. Wu, C. Hwang, "Optimal Design and Control of CPU Heat Sink Processes", *IEEE Transactions on Components and Packaging Technologies*, 31 (1): 184–195, March 2008.

[8] P.R. Spalart, S.R. Allmaras, "A one-equation turbulence model for aerodynamic flows", *AIAA-Paper 92-0439*, 1: 5–21, 1992.

[9] J. Vierendeels, L. Lanoye, J. Degroote, P. Verdonck, "Implicit coupling of partitioned fluid-structure interaction problems with reduced order models", *Computers and Structures*, 85(11–14): 970–976, 2007.

[10] G. Golub, C. Van Loan, *Matrix computations*, Johns Hopkins University Press, Baltimore, MD, USA, 3 edition, 1996.